RESEARCH ARTICLE | DECEMBER 29 2021

Tunable plasmon–polarizmon resonance and hotspots in metal–silicon core–shell nanostructures

Special Collection: 2021 Energy

Ammar Nayfeh; Ayman Rezk ; Noha Elhalawany; Majid Al Ruqeishi ; Adem Kocyigit; Ersin Bahceci ; Munir Hasan Nayfeh

AIP Advances 11, 125129 (2021)
https://doi.org/10.1063/5.0077841

Tunable plasmon–polarizmon resonance and hotspots in metal–silicon core–shell nanostructures

Cite as: AIP Advances 11, 125129 (2021); doi: 10.1063/5.0077841
Submitted: 7 November 2021 • Accepted: 7 December 2021 •
Published Online: 29 December 2021

Ammar Nayfeh,[1] Ayman Rezk,[1] Noha Elhalawany,[2] Majid Al Ruqeishi,[3] Adem Kocyigit,[4] Ersin Bahceci,[5] and Munir Hasan Nayfeh[6a)]

AFFILIATIONS

[1] Electrical Engineering and Computer Science, Khalifa University, Abu Dhabi 127788, United Arab Emirates
[2] Polymers and Pigments Department, National Research Center, 12622 Cairo, Egypt
[3] Mathematical and Physical Sciences Department, College of Sciences and Arts, University of Nizwa, 33616 Nizwa, Oman
[4] Electronic Communication Technology, Bilecik Seyh Edebali University, 11100 Bilecik, Turkey
[5] Department of Metallurgical and Materials Engineering, Iskenderun Technical University, 31200 İskenderun, Hatay, Turkey
[6] Department of Physics, University of Illinois at Urbana-Champaign, 1110 W. Green Street, Urbana, Illinois 61801, USA

[a)] **Author to whom correspondence should be addressed:** m-nayfeh@illinois.edu

ABSTRACT

Metal nanostructures create near-field super hotspots under light irradiation with a range limited to a few nanometers. The intense field in the spot affords enhanced nonlinear optical processes, such as Raman spectroscopy. The intense field, however, can cause heavy distortion and thermal damage to the molecular specimen as well as heavy convolution with the metal electronic structure. In this work, we simulate concentric layered silicon–metal core–shell (and its inverse) nanostructures that may alleviate the disadvantages of the pure metal environment. Our results using Mie and finite-difference time-domain scattering studies show that, in addition to the super hotspot at the gold–silicon interface, there emerges a super hotspot at the silicon–vacuum interface, whose intensities anti-correlate and are tuned by tuning the silicon thickness. Moreover, the plasmonic resonance red shifts with the thickness of the silicon shell, reaching a terminal wavelength of ~840 nm. These features are understood in terms of induced polarization charge at the silicon–metal and silicon–vacuum interfaces, which for high κ materials (13.32) can be significant. The metal–silicon system creates plasmon–polarizmon hotspots tunable in strength and wavelength content that can be designed to alleviate high field damage, useful for Raman scattering and photovoltaic applications. The integrated metal–silicon system also promises field enhancement of visible luminescence of silicon nanoparticles, useful for imaging and tracking applications.

I. INTRODUCTION

Surface enhanced Raman scattering (SERS)[1,2] provides increases in scattering cross sections of an external light (laser light, for example) by sample molecules of several orders of magnitude when the molecules are placed within atomic distances from sharp nanoscale metal structures. The process affords enhanced sensitivity of vibration fingerprint recognition by the otherwise highly weak Raman spectroscopy. The enhanced scattering/sensitivity arises from the ability of metal nanostructures to focus the incident light of certain wavelengths (in the visible for gold) to a small spatial nanoregion (hotspot) within a few nanometers from the metal nanostructures.[3,4] The focusing stems from resonance excitation/emission by oscillations of "free" electrons in the conduction band of the nanometal. In the hotspot, a molecule will be subjected to a much stronger electric field than that of the incident field. The Raman response becomes highly enhanced as the process has a quartic (fourth power E^4) dependence on the light field.[5–7] The enhanced process, however, includes some major disadvantages. For instance, absorption and dissipation processes in metals can lead to

the release of heat (plasmonic heat) due to charge motion, which can alter or decompose the molecular sample causing unwanted modifications.[8–10]

In recent years, nano-structured dielectrics and semiconductors have been proposed as non-plasmonic or plasmon-free alternative materials to metals[11–18] to alleviate strong electronic coupling, nonlinear structural deformations, and thermal damage. Studies using semiconductor nanoparticles showed an enhancement in the Raman signal of adsorbed molecules;[19–21] however, it was considerably lower than those for metals, which was attributed to the inaccessibility of the plasmon resonance. It would be interesting to examine an intermediate solution that combines good attributes of a metal and semiconductor in the same system, such as tailoring a layered metal–dielectric (thin film of Si nanoparticles),[22–26] that may soften the enhancement of the Raman scattering to alleviate strong field effects while keeping a moderate enhancement. Moreover, one needs to examine different designs of material layering to check if indeed the integration would afford wavelength tunability and operation in the visible as well as in the near infrared regions. Moreover, it may be possible to provide an opportunity to use the plasmonic field to enhance the pumping of nanosolids of luminescent silicon nanoparticles that may increase their brightness. However, it is not clear if the high conductivity shielding of a metal can be overcome to attain a strong enough coupling between various metal and semiconductor layers.

In the simulation studies, we employ Mie scattering formalism[27–29] as well as three-dimensional finite-difference time-domain (3D-FDTD)[30,31] to calculate the wavelength dependence of near-field electric field distribution and map out the resonance frequencies over the range from the vacuum UV to the infrared. We consider specific core–shell architectures in which synergetic functionalities emerge upon integration of nanometal and silicon. The studies focus on concentric metal–silicon core–shell architectures with the metal constituting the core and the shell consisting of closely packed luminescent silicon nanoparticles. We also examine the inverse core–shell architecture. Studies of the response of these architectures with a variable silicon and metal thickness to determine the appropriate design thickness of the various layers to achieve good coupling to offset the high conductivity shielding of metal can be done to attain strong enough coupling between metal and semiconductor layering.

The results show that the gold plasmonic resonance at 500 nm red shifts monotonically with the thickness of the silicon shell reaching a terminal wavelength of ~840 nm. In addition to the super hotspot, soft hotspots appear at the silicon–vacuum interface with an overlap between the hotspots tunable by controlling the thickness of the silicon shell in the inverse core–shell architecture case. As the metal thickness is decreased from T (~20 nm) > δ the skin depth, the strength of the plasmon resonance drops (but the position remains pinned at ~500 nm), while a resonance associated with Si emerges and shifts from 550 to ~1500 nm at T << δ, becoming much stronger than the plasmon resonance at 0.3 nm. At an intermediate thickness of 5–6 nm, the strength of the hotspots is comparable (with ~80 nm^2 cross section and reflectivity–transmittivity). The infrared resonant activity is understood in terms of induced polarization charge at the silicon–metal and vacuum surface interfaces, which for high κ (13.32) can be significant. The metal–silicon system creates infrared, tunable, and softer plasmon–polarizmon hotspots, useful for Raman scattering. The integrated metal–silicon also promises field enhancement of visible luminescence of silicon nanoparticles, useful for imaging and tracking applications.

II. MIE SCATTERING

In this section, we conducted Mie scattering[27–29] studies. We examined individual silicon nanoparticles as well as closely packed clusters of the particles. The study involves direct analytical solution of Maxwell's equations of particles in the presence of electromagnetic fields **E** and **B** using series expansions of the involved fields into partial waves of different spherical symmetries to model the interaction of metal–semiconductor nanoparticles with electromagnetic radiation. We calculated the electromagnetic field Mie scattering for two concentric core–shell structures of metal and silicon, namely, a gold nanoparticle coated with a thin silicon layer consisting of closely packed silicon nanoparticles, and the inverse structure in which there is a silicon–core consisting of a cluster of silicon nanoparticles with a thin gold coating layer. We first studied the configuration of a gold nanoparticle of radius *a* with a silicon shell of thickness *b*–*a* coating as shown in Fig. 1. The diameter of the gold nanoparticle used in those studies is 2a = 7 nm. This is a model configuration to illustrate and display some characteristics. It represents closely packed H-terminated particles with each having a Si–H monolayer termination of 1-Å bond length. Hydrophobic forces in an aqueous environment drive the particles. Hydrophobic forces can make colloidal crystals with closely packed particles, some of which would nucleate on the plasmonic structure. The particle distribution of the nanoparticles is expected to be random but reasonably uniform. This provides an interparticle atomic scale gap of 3 Å, with a density of the order 10^{12}–10^{13} cm^2. For a gold nanoparticle of 7-nm diameter, a total of ~20 particles of 3 nm diameter is expected for a single monolayer.

The Mie scattering study is for a silicon shell of thickness 0, 1, 1.5, 2, 7, 10, and 15 nm. Gold nanoparticles present in an infinite silicon medium are equivalent to taking the outer dimension b to infinity ($b \rightarrow \infty$). Figures 2(a)–2(d) give a subset of the spectra for silicon thicknesses of 0, 1, 7, and 10 nm. It shows that the gold plasmonic resonance without a silicon coating at 500 nm gets stronger and red shifts monotonically with the thickness of the silicon shell reaching a terminal wavelength of ~840 nm. With no silicon coating, the scattering cross section is 6 nm^2 and it grows to 52 nm^2 for a silicon thickness of 15 nm. In the limit of infinitely thick coating, i.e., for an infinite medium, the cross section grows to 350 nm^2. At the same time, the resonance shifts from 500 nm without a silicon coating to 830 nm for 15-nm thick silicon coating and to 840 nm for infinitely thick silicon coating. Table I summarizes the results of more cases of those Mie scattering calculations (gold nanoparticles with 7 nm diameter with a silicon shell of increasing thickness), giving the resonance wavelength λ_r (nm) as well as the cross section σ_r (nm^2) at resonance for different thicknesses of the silicon shell.

We examined gold particles with diameters of 10, 20, 30, and 40 when the silicon thickness is >15 nm. The results are given in Figs. 3(a)–3(d), respectively. The figures show that the spectra do not shift significantly with size. They shift by ~10% (from ~840 to 930 nm) with some broadening FWHM from ~50–125 nm over the diameter range of 10–40 nm, respectively.

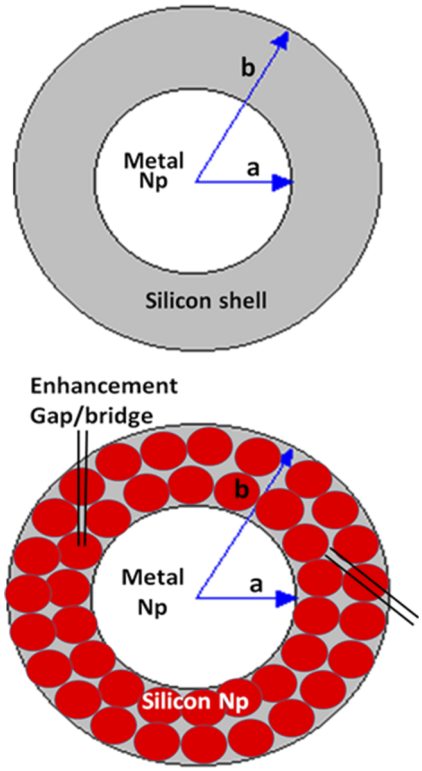

FIG. 1. Configuration of a gold nanoparticle of radius *a* with a silicon shell of thickness *b*–*a* (coating).

TABLE I. Mie scattering of gold nanoparticles of 7 nm diameter with a silicon shell.

Si shell thickness t (nm)	Resonance wavelength λ_r (nm)	Resonance cross section σ_r (nm^2)
0	500	6
1	600	25
2	675	48
4	770	51
7	810	48
10	825	50
15	830	52
∞	840	350

To elucidate the effect of integration, we analyzed the above case of 7 nm diameter gold core and a silicon shell thickness of 1.5 nm by calculating the plasmon frequency of each constituent separately. Figures 4(a)–4(c) show the Mie scattering cross section for the gold sphere, and the silicon shell individually, and the integrated system, respectively. The gold response in Fig. 4(a) shows an electric dipole plasmon resonance at 504 nm, magnetic dipole plasmon resonance at 350 nm, and electric quadrupole plasmon resonance at 208 nm, with cross sections in the ratio of 6:4.2:9.5, respectively. The resonances are wide enough such that they have some overlap. The freestanding silicon shell in Fig. 4(b) does not show any resonance response in this range. The layered integrated response in Fig. 4(c) shows a number of interesting features. The higher monopole resonances shift somewhat to a longer wavelength but most importantly, their cross sections are diminished drastically by more than a factor of 10 and 15, respectively. The electric dipole resonance shifts to

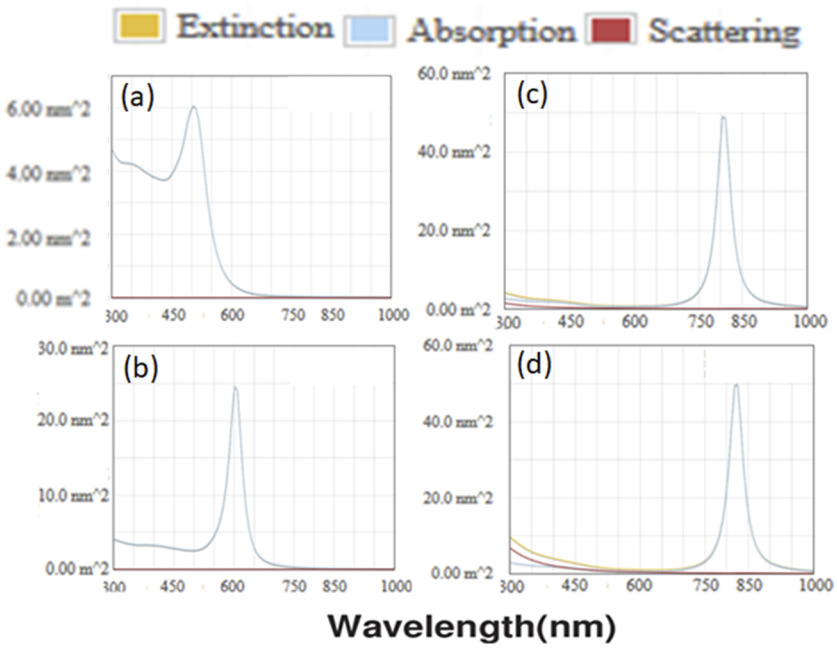

FIG. 2. (a)–(d) Mie scattering for a gold nanoparticle of 7-nm diameter with a uniform coating layer consisting of silicon of thickness 0, 1, 7, and 10 nm, respectively.

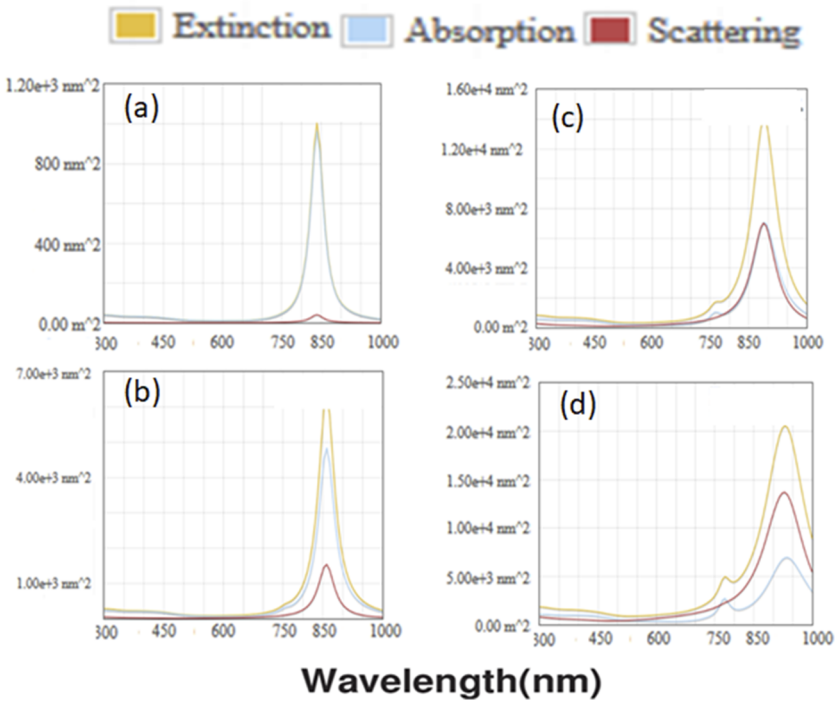

FIG. 3. Mie scattering cross section as a function of incident wavelength for different gold nanoparticle diameters. (a)–(d) 10, 20, 30, and 40 nm, respectively. The silicon thickness is very large. (The gold particles are effectively embedded in an infinite silicon medium.)

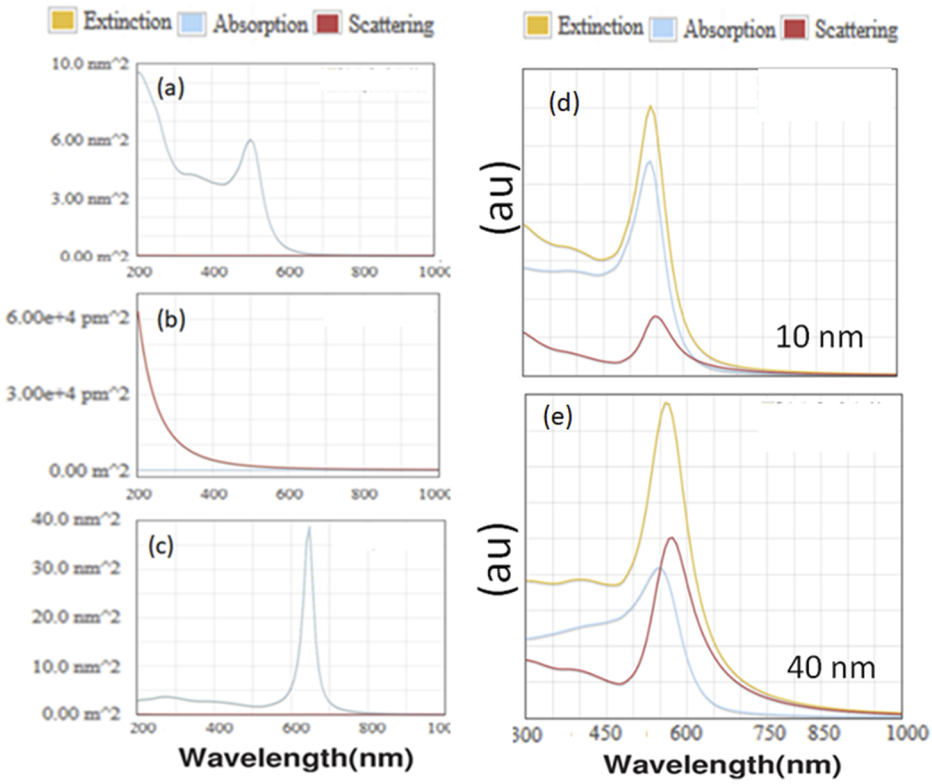

FIG. 4. Mie scattering of gold–silicon core–shell structures embedded in a 1.33 refractive index medium (water). (a)–(c) Spectra and cross section for a 7 nm diameter gold particle, and a 1.5 nm thick silicon shell individually, and the integrated system, respectively. (d) and (e) Spectra for 10 and 40 nm diameter gold particles, respectively, with no shells.

longer wavelengths by nearly 145 nm from 504 to 648 nm as well as gets narrower by about a factor of 1/2, while its cross section at the maximum grows by an order of magnitude from 4 to 40 nm^2. We also examined the stability of the plasmon resonance (position and width) of a pure spherical gold structure. Figures 4(d) and 4(e) show the Mie scattering cross section for gold particles (without a silicon shell) of different diameters. The response for a diameter of 10 nm given in Fig. 4(d) shows an electric dipole plasmon resonance at 545 nm. Figure 4(e) shows the corresponding gold resonance for a diameter of 40 nm, showing also an electric dipole plasmon resonance with little shift to ~505 nm or change in width from that for the 10 nm case.

In addition, we studied the inverse core–shell structure in which the core consists of a closely packed cluster of silicon nanoparticles, while the shell is a metal coating as shown in Fig. 5. The thickness of the metal coating is fixed, while the silicon nanoparticle core is taken with different sizes. We calculated the Mie scattering spectrum of the electromagnetic field for a thin 1-nm gold layer (shell). The spectrum generally consists of two resonances at λ_p and λ_i. Table II summarizes the results of the calculations for a core with 1, 1.67, 2.2, 2.9, 3.7, 5.0, 10, 20, and 25 nm diameters, giving the resonance wavelength λ_p (nm) and λ_i (nm) as well as the corresponding cross sections σ_p (nm^2) and σ_i (nm^2) for the various diameters of the silicon core. Figures 6(a)–6(d) show the scattering spectra for a subset of these cases including 1, 1.67, 10, and 20 nm diameter cores,

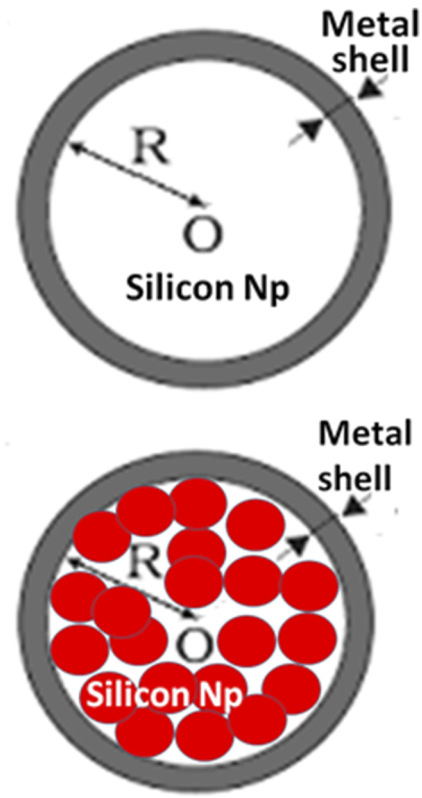

FIG. 5. Configuration of the inverse core–shell structure in which a silicon nanoparticle cluster of radius R constitutes the core and a gold shell.

TABLE II. Mie scattering of a 1 nm thick gold nanoshell with a silicon nanoparticle fill.

Si nanoparticle diameter (nm)	Resonance wavelength λ_p, λ_i (nm)	Resonance cross section σ_p, σ_i (nm^2)
1 (air)	510, none	0.52, none
1	500, 590	0.4, 0.29
1.67	500, 600	0.55, 0.94
2.2	500, 610	0.67, 1.8
2.9	500, 650	0.85, 4.35
3.7	500, 700	1, 7.7
5	500, 760	1.5, 14
7	500, 850	2, 28.8
10	500, 900	4, 55
15	500, 1150	7, 108
20	500, 1300	10, 187
25	500,1440	17, 295

respectively. Each spectrum exhibits two resonances. We associate the higher frequency peak at λ_p with the plasmonic response, while the lower frequency peak λ_i with the Si nanoparticle component. Note that as the size of the silicon core increases, the corresponding peak monotonically shifts toward the infrared. At the same time, the plasmonic resonance remains pinned but gets diminished relative to that of the silicon core.

The results suggest that for a 1-nm gold thickness, a fraction of the light is able to penetrate the gold shell into the silicon core. At high frequencies, such as visible light, the skin depth of gold is a few nanometers (15–25 nm), significantly smaller than the skin depth at 60 Hz (8.5 mm). To elucidate the role of the thickness of the gold shell, we conducted studies of the Mie scattering for different gold thicknesses. Table III gives Mie scattering of the Si cluster of a fixed diameter (7 nm) with a gold shell of varying thickness ranging from 25 nm down to 0.3 nm.

Table III shows that for a thickness >15 nm, there is only the pure plasmon resonance at 510 nm, indicating that the light is not penetrating the gold shell (near-full shielding). For thinner shells, the resonance remains pinned at ~500 nm, while a second induced resonance at a longer wavelength emerges and keeps shifting reaching ~1400 nm for 0.3 nm. The induced resonance is associated with the excitation of the silicon core by light penetrating the gold shell. As to the strength of the resonances, the cross sections of both resonances drop as the gold thickness is reduced. At a 5–6 nm gold thickness, the cross sections of both resonances become equal with a cross section of ~80 nm^2. For thinner metal shells, the cross section of the plasmonic resonance drops very fast, becoming at 0.3 nm an order of magnitude smaller than that of the induced polarization. Recent calculations showed that for gold the thickness at which a layer's reflectivity, R, becomes equal to its transmittivity, P, with R = P = 0.25 (absorption Q = 0.5) is 1.34 nm.[32] For thin enough metal, the layer would break into isolated "islands." When they are still close to each other, the local field due to the formation of plasmons can get enhanced by orders of magnitude and the closely packed islands may induce tunneling transitions and discharges, i.e., strongly nonlinear effects that may result in high harmonics generation. The process would exhibit some nonlinearity.

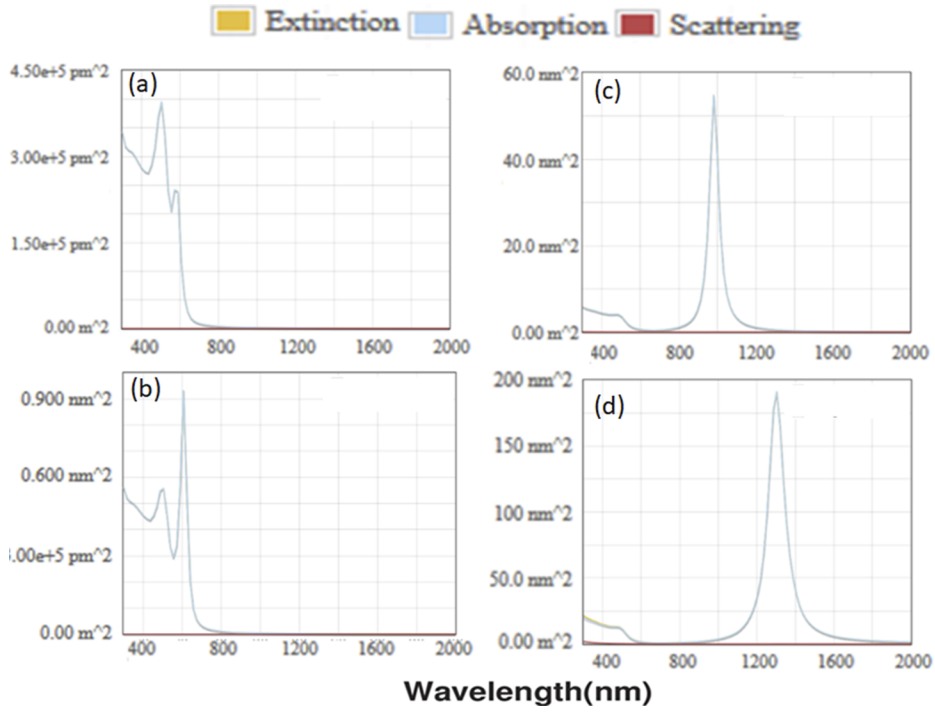

FIG. 6. (a)–(d) Mie scattering of the electromagnetic field for a silicon–core with a thin gold layer (1 nm). The results are shown for a core diameter of 1, 1.67, 10, and 20 nm, respectively.

These features are expected to commence in layers slightly thinner than 1–2 nm.

Since the gold thickness is significantly less than the skin depth, the Faraday cage shielding effect will not be complete, and we expect a sizable fraction of the incident light to travel into the silicon core and polarize. We can estimate the polarization charge density σ_p at the interface just inside the silicon layer in terms of the charge density in the conductor σ using the expression $\sigma_p = \sigma\,(k-1)/k$. Note the dielectric constant k for silicon is k = 13.32 (refractive index 3.65). Hence, $\sigma_p = \sigma\,(k-1)/k = 0.925\,\sigma$. As to the role of plasmon resonances, we can estimate the location of the plasmon resonance (ω_p) using the following expression of the plasmon frequency:[33]

$$\omega_p = \left(\frac{4\pi N e^2}{\varepsilon_\infty m^*}\right)^{1/2}, \tag{1}$$

where m^* is the effective electron mass and N is the electron density. Since N is expected to be small in silicon conduction bands, and since the plasmon frequency is proportional to the square root of N, ω_p is expected to lie deep in the infrared. With a 3-nm particle having a volume $V = 14.1 \times 10^{-21}$ cm^3 even if one electron is promoted to its conduction band, we expect the charge density to be 7×10^{19}/cm^3 in the particle. Using $m^* = 0.25$ m in silicon, and one electron in the conduction band, gives a plasmon resonance at ~8 μm, well beyond the visible region.

For pure gold with a vacuum cavity, the resonance wavelength is 500 nm. Using the electron mass in silicon $m^* = 0.25$ m gives a resonance wavelength of 948 nm, in reasonable agreement with 840 nm, the numerical solution. It is to be noted that for a material with a higher dielectric function, the polarization of the medium increases. The greater polarization of the medium attenuates the accumulated charge in the resonance zone more significantly. Attenuating the electric charge of the NPs reduces the restoring electric force, which reduces (red shifts) the resonance frequency. This can be seen using the simulation based on the Mie theory presented in Figs. 2 and 3 and Tables I and II.

TABLE III. Mie scattering of a 7 nm diameter Si cluster with a varying gold shell.

Au shell thickness t (nm)	Resonance wavelength λ_r (nm)	Resonance cross section σ_r (nm^2)
25	510, 568	4100, 1000
20	510, 564	2200, 560
15	510, 565	933, 308
13	510, 565	650, 230
12	510, 566	527, 180
11	510, 565	421, 150
10	510, 565	331, 132
9	500, 565	250, 118
8	500, 576	192, 103
7	500, 576	140, 88
6	500, 587	97, 82
5	500, 598	63, 74
4	500, 609	38, 68
3	500, 631	20, 62
2	500, 697	8.5, 58
1	500, 851	2.5, 30
0.75	500, 950	1.5, 20
0.5	500, 1115	0.8, 12
0.3	500, 1400	0.43, 7.5

III. FDTD FIELD DISTRIBUTION

The Finite-Difference Time-Domain (FDTD) method is a discrete solution to Maxwell's equations based on central difference approximations of the spatial and temporal derivatives of the curl-equations.[30] The FDTD method used is commercial software (COMSOL MultiPhysics Software® 5.3a AC/DC module electromagnetic waves). In the software, the related simulation parameters in FDTD simulation, e.g., the dimensions of perfectly matched layer (PML) and grid size, are a physics based mesh, with a max element size 0.35 nm and a min element size 0.000 05 nm, maximum growth rate 1.3, curvature factor 0.3, and resolution of narrow regions 1. Using a reflectionless absorbing boundary (PML method) makes the FDTD method capable of simulating unbounded problems. Moreover, the procedure is capable of absorbing evanescent waves and near fields. Another feature, which was made possible by using the basic Yee algorithm, allows the procedure to handle modeling of very complex geometries.[31] This is augmented with the use of sub-cell modeling techniques and local sub-grids. That is, a subgrid is embedded within the global grid in order to locally resolve fine geometric structures without sacrificing the global space/time scale. The applications of sub-cell models and sub-gridding methods have proven to enhance the efficiency and the accuracy of the FDTD method for modeling very complex systems. We apply the FDTD method to the architectures given in Figs. 1 and 5. For a closely packed layer of silicon nanoparticles, the wavelength dependence of the refractive index and the absorption coefficient n and k used in the calculations can be approximated by those of bulk silicon as shown in Fig. 7.[34,35] The model used for the permittivity of the core metal (Au) nanoparticles is the Lorentz–Drude model, i.e., Drude free electron model and Lorentz oscillator model. For instance, k and n are taken from the work of Babar and Weave.[36]

We first apply the FDTD method to the architecture shown in Fig. 1. We use a linearly polarized incident beam of amplitude E_{inc} (or background field E_b) with an amplitude of 1.0 V/m. The incident beam is propagating along the x direction, and the polarization is along the z direction (see the coordinate system in the figure). Usually for the calculations, a plane wave source is desired. The creation

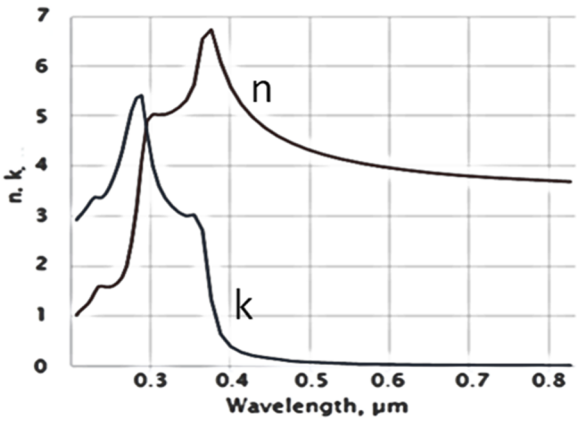

FIG. 7. Wavelength dependence of the optical constants n and k for a closely packed layer of silicon nanoparticles. Those are approximated by thin crystalline silicon.

of this plane wave is what characterizes the difference between the total field and the scattered field in the calculation domain. The scattered field is defined as $E_{sca} = E_{total} - E_{inc}$, where E_{total} is the total field and E_{inc} is the incident field. This definition is enforced at the boundary between the total and scattered fields by adding in or subtracting out a correction term for the update equations on and next to this boundary.

The core–shell structure shown in Fig. 8(a) is a 10-nm total diameter, with a gold core of 7 nm diameter and a silicon shell of a thickness of 1.5 nm. The structure is much smaller than the wavelength in the range 200–1400 nm, and thus, we introduce no spatial variation of the electric field across the nanostructure. Figure 8(b) shows the near-field distribution at an incident wavelength of 600 nm using the color code given on the right of the figure. Observations of the near-field strengths using color coded maps show two hotspots. One of the hotspots is at the gold nanoparticle–silicon interface. The other hotspot is at the silicon–vacuum interface (outer surface of the silicon shell). At the Au–Si interface (inner surface of the shell), the oscillation resonance is due to the combined charge of the gold surface and the silicon polarization charge. These two charge distributions subtract from each other. The second hotspot originates from purely polarization charge. The hotspot phenomenon is a highly local effect occurring at sharp edges, such as the nanostructure considered here, interparticle junctions and crevices, or other geometries with a sharp metal nano-roughness. In Fig. 8(c), we show E_{sca} (the secondary field) lines produced by the re-distribution of the charge in the structure without including the incident field lines, i.e., $E_{total} - E_{inc}$, where as defined above E_{total} is the total electric field and E_{inc} is the incident field.

Figure 9(a) plots the strength of the obtained near electric field with distance from the center of the structure in a direction along the z axis, the direction of the polarization of the incident electric field to display the relative characteristics of the hotspots. Figure 9(b) shows the field strength of the hotspots on both sides of the structure along the z axis. The nature of the charge at the gold–silicon interface is governed by the sum of conduction and polarization charge at the interface. The external field easily separates the charge in the gold nanoparticle. The separated charge polarizes the medium surrounding the gold nanoparticle. The surface conduction electrons in the gold nanoparticle and the polarization charge at the inner silicon surface effectively overlap. Thus, the field due to the polarization applies an opposite force to the restoring force inside the gold, which shifts the resonance to a lower frequency. On the other hand, the conduction electrons in the gold are well separated spatially from polarization charge in the outer surface of the silicon layer. The optical field of the plasmon zone, however, can be seen to overlap with the polarization zone. The plasmon zone bathes nearly the full width of the silicon layer. The highest intensity extends nearly 2 nm, a scale comparable to the radius of the nanoparticle. At the outer edge of the silicon shell, the polarization charge is subjected to the plasmonic electric field of the gold sphere at a strength level of 0.4, about 45 percent of the maximum; hence, they are optically coupled. However, the polarization charge is not chemically or electrically connected to the surface conduction electrons in the gold nanoparticle.

Figures 9(a) and 9(b) also show that the strength of the polarizmon scattered field in the near zone is more delocalized than that of the plasmon zone. This may be attributed to the fact that the former

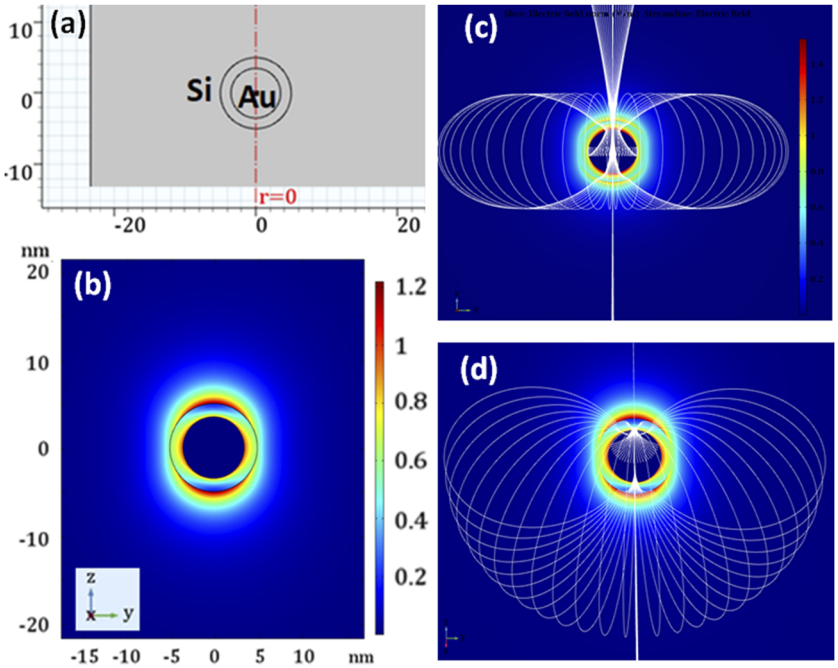

FIG. 8. Core–shell structure of gold nanoparticles with a shell coating of silicon nanoparticles. (a) Cartoon of the configuration of the core (gold) and the shell (silicon). (b) Hotspots in the near-field distribution displayed using the color code given on the right of the figure. (c) and (d) Contours of the scattered electric field lines normalized to those of the incident field strength at an incident wavelength of 600 nm.

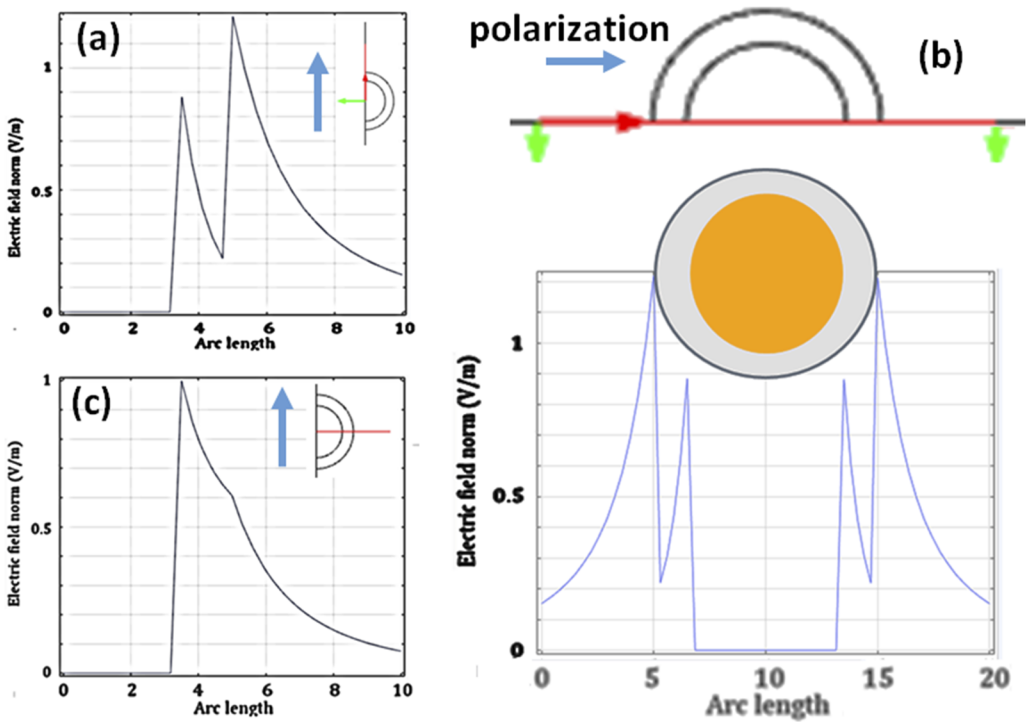

FIG. 9. The strength of the near-field electric with the distance of a gold nanoparticle taken along the polarization of the incident electric field to display the characteristics of the hotspots. (a) From the center of the core–shell to one side and (b) from side to side through the center of the core–shell. (c) From the center of the core–shell to one side and perpendicular to the polarization of the incident electric field. The direction of the polarization is in the direction of the arrow (z direction). The short arrow (green) is in the perpendicular direction of the polarization of the incident field.

is based on neutral dipole atomic fields, whereas the latter is based on bare charge. Figure 9(c) shows the electric field dependence in the direction perpendicular to the polarization. One can see the peak due to the plasmonic hotspot, but there is only a hint of the polarization hotspot. The green arrow is the direction of propagation.

It is to be noted that Fig. 9(a) shows that the polarization resonance at the Si–vacuum interface is stronger than the one at the gold–silicon interface. We examined the relative strength of the fields in the hotspots as a function of the thickness of the silicon shell. Figure 10 shows the field strength as a function of distance for a number of size combinations: (7, 9), (7, 10), and (7, 12) along the color coded intensity for each case. Those correspond to the thicknesses of the silicon layer of 1, 1.5, and, 2.5 nm, respectively. These cases allow us to get the trend of the relative intensities of the plasmon and polarizmon hotspots. The figure shows that we can fine-tune the accessible intensity at the silicon–vacuum by tuning the thickness of the silicon shell. Thus, the core–shell devices allow the conduction of experiments without the specimen molecules coming in contact with the metal surface as well as with a reduced near-field intensity to eliminate any thermal or strong coupling with the substrate.

It is interesting to examine the strength of the hotspots at the silicon–vacuum interface and compare it to that at the gold–silicon interface. We use the results of a core–shell structure consisting of a gold nanoparticle of 9-nm diameter as a core and a silicon coating of varying thickness as a shell. The shell thicknesses studied are 1, 2, 3, and 4 nm. The dependence of the field strength on the distance from the gold nanocore is shown in Figs. 11(a)–11(d), respectively. The images show the hotspots lying along the direction of polarization of the incident light. It is to be noted that the hotspot at the silicon–vacuum interface gets stronger as the silicon coating becomes thinner, overtaking the strength of that at the gold–silicon interface.

The wavelength dependence of the hotspots of the structures discussed above in Fig. 11 is shown in Figs. 12(a)–12(d), respectively. The wavelength range studied is 200–1600 nm (6.2–0.775 eV). One feature we observe is that all structures studied afford good activity in the deep infrared at the hotspot of the silicon–vacuum interface, with the response being nearly smooth with wavelength, except for a hint at the indirect bandgap of silicon at ~1100 nm. The activity in the UV/visible is weaker because of the dip over the band of the gold plasmon. The dip, however, is only 3–10 percent. Thus, these results suggest that by using the appropriate thickness, one can reduce the intensity of the Si–vacuum hotspot to a level below the damage level, i.e., tunable in strength and wavelength content, which can be designed to alleviate high field damages. Moreover, the core–shell devices allow the conduction of experiments without the molecular specimen coming in contact with the metal surface as well as with a reduced near-field intensity, affording elimination of any thermal or strong coupling with metal substrates.

For reference, we obtained distribution at the center of the core structure. Figure 13 shows that the strength of the field amplitude penetrating to the center of the structure is a very small fraction of the scattered field (~4×10^{-3}) at 200 nm, while it is only 3×10^{-4} of the infrared response; it increases as the wavelength decreases. With wavelength, the response may be divided into two regions. The rate of increase in the infrared region 800–1400 nm is much slower than

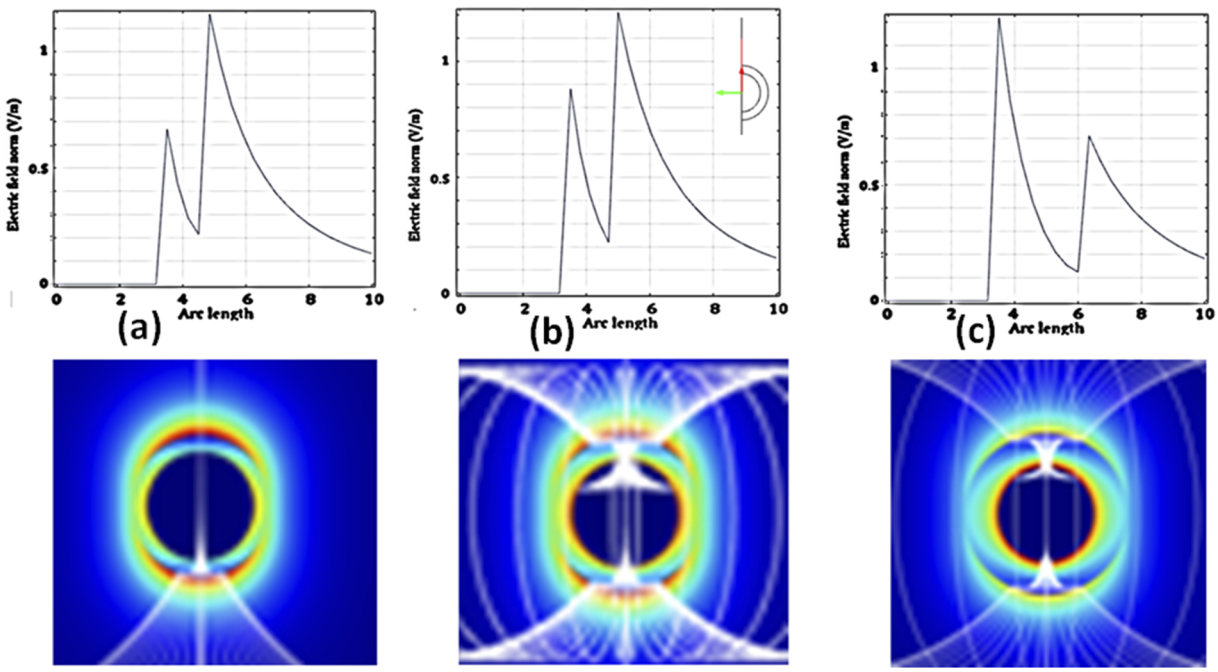

FIG. 10. The relative strength of the fields in the hotspots for different thicknesses of the silicon shell with the size combination (*a*, *b*) of (a) (7, 9), (b) (7, 10), and (c) (7, 12), along with the color coded intensity for each case, corresponding to the thicknesses of the silicon layer (*b*–*a*) of 1, 1.5, and, 2.5 nm, respectively.

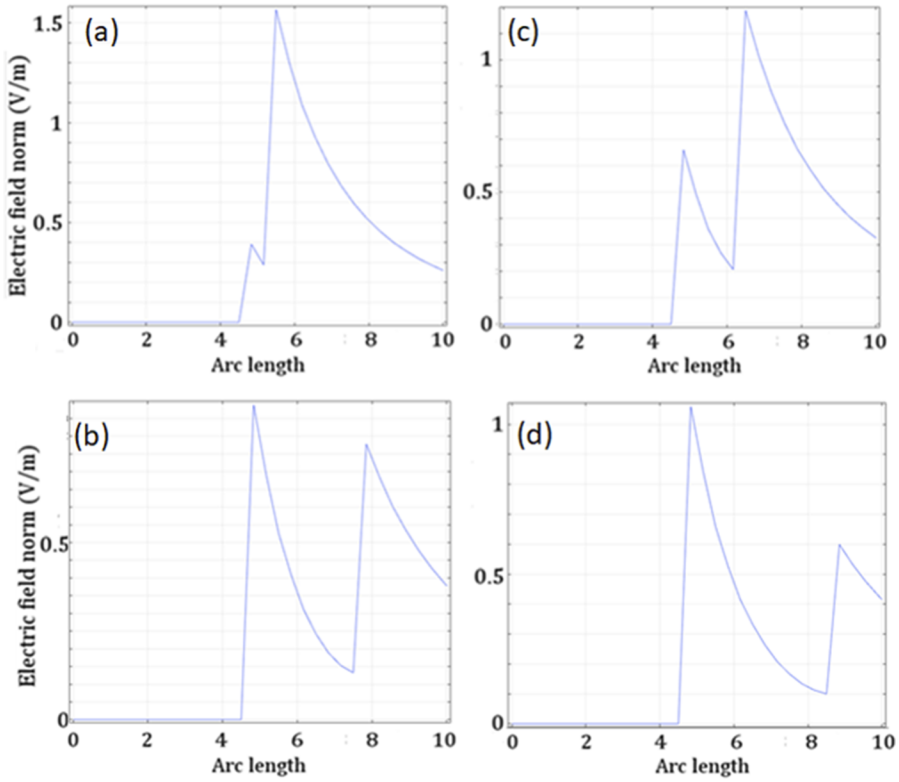

FIG. 11. The dependence of the field strength on the distance from the center of the gold nanocore to the hotspot, along the direction of polarization of the incident light. The core–shell structure consists of a gold nanoparticle of 9 nm diameter as a core and a varying thickness silicon coating as a shell. The shell thicknesses in (a)–(d) are 1, 2, 3, and 4 nm, respectively.

in the visible/UV range 200–600 nm by more than a factor of 25. We also find an increase at 400–500 nm, which is the gold plasmon resonance wavelength for a thinner silicon layer. This is consistent with the fact that the infrared strength in the hotspots is stronger than the visible of the UV content.

The case of a silicon shell made of closely packed luminescent ultrasmall silicon nanoparticles is interesting. In addition to the above hotspots at the inner and outer interfaces, there are expected hotspots in aggregates from adjacent nanoparticle pairs or from highly branched individual nanostructures. Since the particles are luminescent, such enhancement in the near field due to plasmonic effects may strongly excite luminescence. Such high luminescence may be useful in imaging and tracking technologies. In this regard, the stability of near-field nano-optics at hotspots is critical, particularly in a biological milieu. Significant progress in the understanding of the interaction between the excitation electromagnetic field and the surface plasmon modes at the metallic or metallic/dielectric interface of various curvatures is described. New knowledge on methodological strategies for positioning the analytes for SM-SERS and Raman-assisted SERS or the SERS imaging of live cells has been acquired and displayed. In the framework of the extensive development of SM-SERS as an advancing diagnostic analytical technique, the real-time SERS chemical imaging of intracellular compartments and tracing of individual analytes has been achieved. In this context, we highlight the tremendous potential of SERS chemical imaging as a future prospect in SERS and SM-SERS for the prediction and diagnosis of diseases.

FDTD field scattering strength computations were performed for the configuration shown in Fig. 5 with a silicon nanoparticle cluster of 7 nm diameter and with a gold shell of 1.5 nm thickness. Since the gold thickness is significantly less than the skin depth, the Faraday cage effect will not be complete, and we expect a sizable fraction of the incident EM wave to penetrate the gold shell and travel into the silicon material and polarize it (see the discussion of Table III above). Figure 14(a) shows a drawing of the core–shell structure. Figure 14(b) shows the strength of the scatted field in the near zone using a color code format. It is to be noted that the incident field is traveling perpendicular to the page (along the x axis), while the linear polarization is along the z axis. Figure 14(c) also shows some field lines of the secondary field and displays the hotspots created. The strength of the field in the hotspot as a function of the wavelength of the incident field is shown in Fig. 14(d).

The studies give us the opportunity to examine the current interest in integration of electronics and optics[37,38] by integrating silicon with metals especially noble metals, such as gold and silver. The basic mechanism involves subjecting silicon to concentrated plasmonic EM fields. Plasmonic fields within a few nanometers from the metal can approach atomic field strengths, which when applied to Si induces significant distortion in its crystal structure that breaks symmetry and modifies the electronic and optical properties, affording Si, for example, efficient visible photoluminescence, infrared reception, or enhanced coupling to light. The high fields afforded by plasmonic nanometal materials can be comparable to atomic and molecular fields[39,40] and hence cause distortion and modification of the

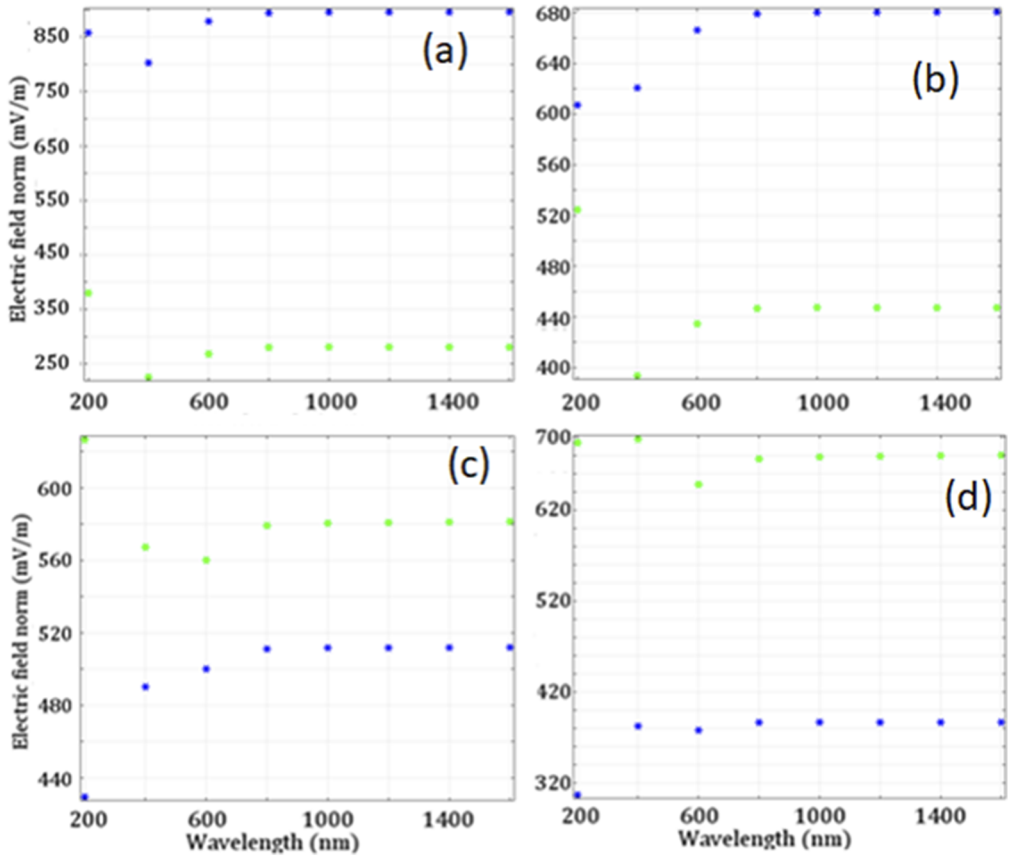

FIG. 12. (a)–(d) Spectral content of the hotspots at the silicon–vacuum interface as well as the gold–silicon interface shown in Figs. 11(a)–11(d) for gold–shell thicknesses of 1, 2, 3, and 4 nm, respectively.

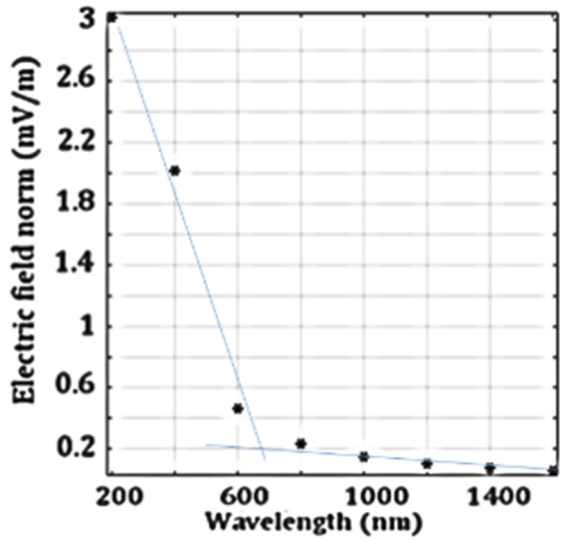

FIG. 13. Ratio of the scattered field intensity to the incident intensity as a function of wavelength in the region 200–1600 nm, evaluated at the center of the structure.

crystal structure, and charge separation (polarization) and hence the interaction with light. Recently, hybrid metal–semiconductor systems have been investigated,[4,41–44] one interesting example in which a pure silicon nanowire wrapped with glass and silver.[41] Subjecting the silver coating to a narrowband blue laser beam, subjected silicon to an intense plasmonic field, which induced the silicon wire to emit white light that spans nearly the full visible spectrum. The broad bandwidth light has good potential for operation in photonic or optoelectronic devices.

Finally, we discuss the feasibility of the realization of the core–shell structures. Silicon nanoparticles were used in charge exchange reactions as a reducer of metal ions to harvest metals or their oxides, such as erbium, magnesium, iron, and gold.[26,45–50] For example, when magnesium chloride salt in water is reacted with H-terminated Si nanoparticles of 2.9-nm diameter in isopropanol alcohol, the Mg^{2+} ions and clusters of nanoparticles are attracted to each other by polarization forces, followed by exchange of holes from Mg^{2+} to oxidize silicon. The reduced Mg or its oxide form forms a solid precipitate coating the Si grains. H-terminated Si nanoparticles are also able to reduce erbium, magnesium, iron, and gold ions to their metal forms because silicon nanoparticles have electronegativity larger than those of metals, i.e., larger reduction potential,

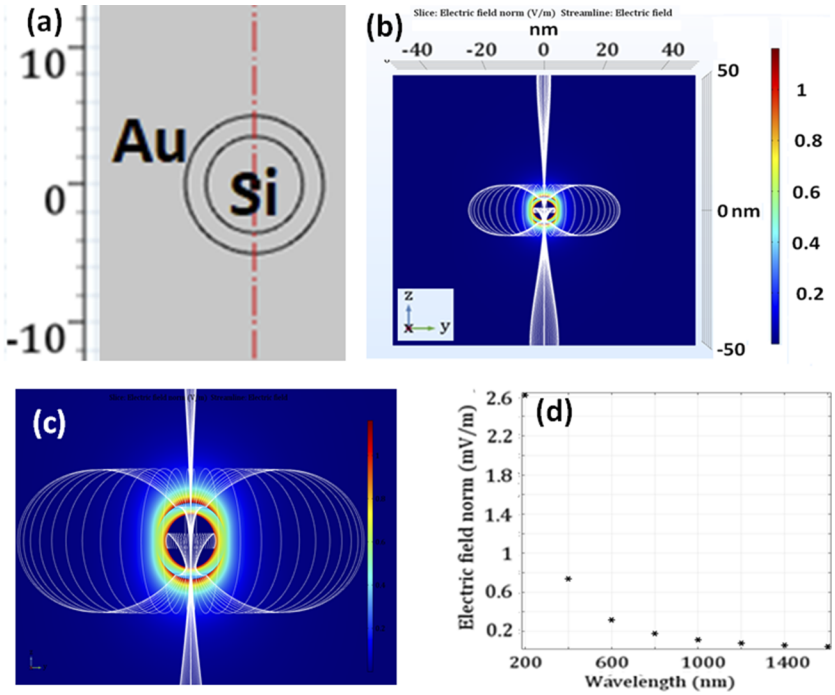

FIG. 14. (a) Cartoon of the inverse structure: core (silicon) and shell (metal). (b) Hotspot strength of the scattered field in the near zone using a color code format. (c) Field lines of the secondary field. (d) Strength of the field in the hotspot as a function of the wavelength of the incident field.

which favors exchange of holes or electrons. In these reactions, the photoluminescence of the Si nanoparticles showed stability, and thus Si(0) is not consumed, while the shell may have provided protective cladding against luminescence quenching.

On the other hand, one might be able to coat gold nanoparticles with silicon. The method includes physical procedures, such as metal-assisted chemical vapor deposition (CVD) synthesis.[51–53] It works in a gas environment. Vapor–liquid–solid (VLS) growth is a type of catalyzed CVD, which often uses silane as a Si precursor and heated gold nanoparticles as a catalyst (or "seed").

IV. DISCUSSION

We should note that the present study aims at softening the plasmonic field in the near-field hotspots or creating new softer hotspots by integrating plasmonic metal (Au, Ag, and Cu) and non-plasmonic metal or dielectric material (such as silicon and silicon oxide) in convenient architectures. The interest in this direction stems from a desire to make extremely small samples of highly sensitive, bio-medically important molecules, such as DNA amenable to SERS by reducing damage or strong electronic convolution with the active nanostructure. However, there remains, for certain applications, strong interest in strengthening the plasmonic field in the hotspots of plasmonic metals[54–64] as well as enhancing the hotspots of non-plasmonic metals, such as the transition metals like Pt, Pd, Ru, etc., metals in use in catalytic applications.[55] Transition metals and other nonmetal materials that are usually used in catalysis (material limitation) are almost impossible to employ in SERS-based applications. The suggested architectural schemes include core–shell of spherical as well as non-spherical geometries, such as triangular, pyramidal, nanorods, sheets, or irregular complex geometries.[63,64] Moreover, gap fields created by the proximity of multiple nanostructures have been under research and applications.[21,60,61] Moreover, integration of nanoarchitectures of different plasmonic active materials and non-plasmonic materials in complex geometries has been finding a myriad of new applications, ranging from analytical material sensing to optical antennas to refractive index sensors.[21,62–64]

The SERS activity transcends application. There is presently a concerted effort to study the fundamentals of the optical properties of nanometals for better understanding of the phenomenon, which in turn would facilitate the realization of the full potential of SERS in advanced and emerging applications in plasmonics, nanoscience, and nanotechnology. It is, in fact, imperative to discern the fundamental properties of metals and the effect of different types of matrix environment at the nanoscale to allow better device optimization and material/geometrical design and integration. Embedding, integrating, or coating metal nanostructures with other materials affects the frequencies, strength, and damping of the plasmonic resonances.

Detailed classical theory of the dispersion relation for the plasmon waves involves the solution of divergent free Maxwell equations (no external charge, current sources, or incoming light wave).[65] The equations are first reduced to the Helmholtz homogeneous wave equations. In the procedure, the vector solutions of the Helmholtz equations in two homogeneous regions inside and outside the sphere are expressed as a sum of infinite series of spherical multipole partial waves of order l,[66] according to the formalism of Mie scattering theory.[27] The continuity relations at $r = R$ for the tangential components of the transverse magnetic (TM) EM modes (with non-vanishing electric field component normal to the interface) lead to non-trivial solutions under certain conditions. Basic

optical properties of small particles can be explained satisfactorily by this classical EM theory using the bulk-type dielectric function (DF). Realistic representation of the frequency dependence of the dielectric function of noble metals has a significant impact on the accuracy of description of their optical properties. The fundamental optical characteristics of pure gold nanoparticles in an infinite water medium were recently obtained by semi-analytical solution of a model that uses the Druse–Sommerfeld model with modification of the DF to include corrections for the interband transition in gold at 1.8 and 2.4 eV.[65] The multipolar (e.g., dipole and higher order polarity, i.e., l = 1–5) plasmon resonance frequencies and damping rates (eigenmode solution), with retardation effects taken into account, has been obtained as a smooth function of the particle radius for various indices of refraction for the particle's environment.[65]

The calculated plasmon frequency as a function of the radius of the gold nanoparticle was obtained for several multipoles over the range of size from single nanometers to hundreds of nanometers (<1000 nm). Initially for the electric dipole (l = 1), the frequency of the dipole resonance increases with radius reduction but in the ultrasmall regime, the response flattens out and in fact it drops by ~7% for diameters of 10–40 nm, making the size dependence weak in the optical range. In the study, the red shift in the larger size range (>50 nm) increases more rapidly with increasing R due to EM retardation. The study also shows that the damping dependence on the size of the metal particle is more complicated. The results show that damping/width in the size regime of interest (10–40 nm diameter) decreases by nearly 10%. Our Mie scattering response of pure gold, with no silicon shell, embedded in water is shown in Figs. 4(d) and 4(e) for a gold diameter of 10 and 40 nm, respectively. Both show an electric dipole plasmon resonance at 540 nm with little shift or change in width. The shift from the green to the infrared and slight shift of the position as well as the width with size in the core–shell structure (shown in Figs. 3(a)–3(d) for the core–shell structure) are due to the silicon coating/shell.

V. CONCLUSION

We conduct Mie and FDTD scattering studies from metal nanoparticles coated with nanofilms of silicon (metal–Si core–shell architecture) as well as silicon nanoparticles coated with an ultrathin nanofilm (1 nm) of metal with a thickness below the skin depth of the metal (Si–metal core–shell architecture). For the metal core case, the result shows a resonance at 500 nm that red shifts and increases strength monotonically with increasing thickness of the silicon shell reaching a terminal wavelength of ~840 nm. For the silicon nanoparticle core configuration, the system shows two resonances; one is pinned at 500 nm, and the other red shifts and increases in strength with increasing diameter of the silicon nanoparticle core. The resulting red-infrared resonant proactivity is understood in terms of induced polarization charge density at the metal–silicon surface interface, which for high κ (13.32) approaches that of the metal surface density and effectively creates a tunable plasmon–polarizmon resonance. The integrated plasmonics of metal in silicon might be useful for amplifying the visible luminescence of ultrasmall silicon nanoparticles and for improving light coupling for enhancement of solar cells.

AUTHOR DECLARATIONS

Conflict of Interest

The authors have no conflicts of interest to declare.

DATA AVAILABILITY

The data that support the findings of this study are available from the corresponding author upon reasonable request.

REFERENCES

[1] M. Fleischmann, P. J. Hendra, and A. J. McQuillan, Chem. Phys. Lett. **26**(2), 163 (1974).
[2] R. Signorini, C. Durante, L. Orian, M. Bhamidipati, and L. Fabris, Biosensors **9**, 57 (2019).
[3] D. Pines and D. Bohm, Phys. Rev. **85**(2), 338 (1952).
[4] M. H. Nayfeh, in *Optics in Our Time*, Optics in Nanotechnology, edited by M. Alamri, M. M. El Gomati, and M. S. Zubairy (Springer, 2016), pp. 223–264.
[5] E. J. Blackie, E. C. Le Ru, M. Meyer, and P. G. Etchegoin, J. Phys. Chem. C **111**(37), 13794 (2007).
[6] S. Nie and S. R. Emory, Science **275**(5303), 1102 (1997).
[7] E. C. Le Ru, M. Meyer, and P. G. Etchegoin, J. Phys. Chem. B **110**(4), 1944 (2006).
[8] M. Mahmoudi, S. E. Lohse, C. J. Murphy, A. Fathizadeh, A. Montazeri, and K. S. Suslick, "Variation of protein corona composition of gold nanoparticles following plasmonic heating," Nano Lett. **14**, 6 (2014).
[9] E. C. Le Ru and P. G. Etchegoin, *Principles of Surface-Enhanced Raman Spectroscopy: And Related Plasmonic Effects* (Elsevier, Amsterdam, The Netherlands, 2000).
[10] D. Radziuk and H. Moehwald, Phys. Chem. Chem. Phys. **17**, 21072 (2015).
[11] I. Alessandri and J. R. Lombardi, Chem. Rev. **116**, 14921 (2016).
[12] P. R. West, S. Ishii, G. V. Naik, N. K. Emani, V. M. Shalaev, and A. Boltasseva, Laser Photonics Rev. **4**, 795–808 (2010).
[13] G. V. Naik, V. M. Shalaev, and A. Boltasseva, Adv. Mater. **25**, 3264 (2013).
[14] G. Demirel, H. Usta, M. Yilmaz, M. Celik, H. A. Alidagi, and F. Buyukserin, J. Mater. Chem. C **6**, 5314 (2018).
[15] W. Ji, B. Zhao, and Y. Ozaki, J. Raman Spectrosc. **47**, 51 (2016).
[16] X. X. Han, W. Ji, B. Zhao, and Y. Ozaki, Nanoscale **9**, 4847 (2017).
[17] J. R. Lombardi and R. L. Birke, J. Phys. Chem. C **118**, 11120 (2014).
[18] H. Yamada, Y. Yamamoto, and N. Tani, Chem. Phys. Lett. **86**, 397–400 (1982).
[19] L. G. Quagliano, J. Am. Chem. Soc. **126**, 7393–7398 (2004).
[20] I. Allessandri and J. R. Lombardi, Front. Chem. **8**, 63 (2020).
[21] K. Mantey, L. Quagliano, A. Rezk, S. Palleschi, L. Abuhassan, A. Nayfeh, E. Bahceci, and M. H. Nayfeh, AIP Adv. **11**, 105206 (2021).
[22] O. Ackakir, J. Therrien, G. Belomoin, N. Barry, J. Muller, E. Gratton, and M. Nayfeh, Appl. Phys. Lett. **76**, 1857 (2000).
[23] G. Belomoin, J. Therrien, A. Smith, S. Rao, R. Twesten, S. Chaieb, M. H. Nayfeh, L. Wagner, and L. Mitas, Appl. Phys. Lett. **80**, 841 (2002).
[24] D. Nielsen, L. Abuhassan, M. Alchihabi, A. Al-Muhanna, J. Host, and M. H. Nayfeh, J. Appl. Phys. **101**, 114302 (2007).
[25] M. H. Nayfeh and L. Mitas, "Silicon nanoparticles: New photonic and electronic material at the transition between solid and molecule," in *Nanosilicon*, edited by V. Kumar (Elsevier, 2007), Vol. 1.
[26] M. H. Nayfeh, *Fundamentals and Applications of Nano Silicon in Plasmonics and Fullerenes: Current and Future Trends* (Elsevier, 2018).
[27] G. Mie, Ann. Phys. **330**, 377 (1908).
[28] Nanocomposix, link: https://nanocomposix.com/pages/tools, 2021.
[29] G. Baou, J. Phys. Chem. C **119**, 28586–28596 (2015).
[30] S. Tanev, J. Pond, P. Paddon, and V. V. Tuchin, Adv. Opt. Technol. **2008**, 727418.
[31] K. Yee, IEEE Trans. Antennas Propag. **14**(3), 302 (1966).
[32] A. E. Kaplan, J. Opt. Soc. Am. B **35**, 1328 (2018).

[33]C. Kittel, A. Zettl, and P. McEuen, *Introduction to Solid State Physics* (John Wiley & Sons, New York, 2004).
[34]A. Rezk, S. A. Hadi, J. M. Ashraf, A. Alhammadi, W. Alnaqbi, A. Kumar, G. Dushaq, M. S. Rasras, K. C. Saraswat, M. Nayfeh, and A. Nayfeh, ACS Appl. Nano Mater. **4**(5), 4602 (2021).
[35]Z. Yamani, A. Alaql, J. Therrien, O. Nayfeh, and M. Nayfeh, Appl. Phys. Lett. **74**, 3483–3485 (1999).
[36]J. M. Therrien, "Size dependence of the electrical characteristics of silicon nanoparticles," Ph.D. thesis, University of Illinois at Urbana-Champaign, 2002.
[37]O. Vaughan, Nat. Electron. **1**, 262 (2018).
[38]A. H. Atabaki, S. Moazeni, F. Pavanello, H. Gevorgyan, J. Notaros, L. Alloatti, M. T. Wade, C. Sun, S. A. Kruger, H. Meng, K. Al Qubaisi, I. Wang, B. Zhang, A. Khilo, C. V. Baiocco, M. Popovic, V. Stojanovic, and R. Ram, Nature **556**(7701), 349 (2018).
[39]C. A. Nicholaides, M. H. Nayfeh, and C. W. Clark, *Atoms in Strong Fields* (Plenum Press, New York, 1990).
[40]W. L. Glab and M. H. Nayfeh, Phys. Rev. A **31**, 530 (1985).
[41]C.-H. Cho, C. O. Aspetti, J. Park, and R. Agarwal, Nat. Photonics **7**, 285 (2013).
[42]E. Lerner, https://penntoday.upenn.edu/news/penn-engineers-enable-bulk-silicon-emit-visible-light-first-time, 2013.
[43]B. Piccione, C. O. Aspetti, C.-H. Cho, and R. Agarwal, Rep. Prog. Phys. **77**, 086401 (2014).
[44]Z. Gu, S. Liu, S. Sun, K. Wang, Q. Lyu, S. Xiao, and Q. Song, Sci. Rep. **5**, 9171 (2015).
[45]T. Hoang, N. Elhalawany, B. Enders, E. Bahceci, L. Abuhassan, and M. H. Nayfeh, Appl. Phys. Lett. **109**, 261103 (2016).
[46]A. Kocyigit, N. Elhalawany, E. Bahceci, B. Enders, K. Puthalath, L. Abuhassan, Z. Yamani, and M. Nayfeh, AIP Adv. **8**, 055324 (2018).
[47]N. Elhalawany, K. Mantey, T. Hoang, E. Bahceci, J. Xu, H. Ates, D. Gorin, Z. Yamani, and M. H. Nayfeh, AIP Adv. **10**, 055221 (2020).
[48]E. Bahceci, B. Enders, Z. Yamani, S. Tokmoldin, A. Taukenov, L. Abuhassan, and M. Nayfeh, AIP Adv. **9**, 055228 (2019).
[49]B. Enders, A. Kocyigit, E. Bahceci, N. Elhalawany, A. Nayfeh, O. Alshammari, M. Alsalhi, and M. Nayfeh, AIP Adv. **9**, 095039 (2019).
[50]N. Elhalawany, B. Enders, E. Bahceci, and M. H. Nayfeh, Mater. Phys. Chem. **1**(2), 1 (2019).
[51]R. C. Johnson, http://www.eetimes.com/document.asp?doc_id=1141299, 2000.
[52]L. Xiong, S. Shen, L. Liu, and L. Zhang, Ind. Eng. Chem. Res. **53**, 16672 (2014).
[53]O. M. Nayfeh, D. A. Antoniadis, S. Boles, C. Ho, and C. V. Thompson, Small **5**(21), 2440 (2009).
[54]H. Zhang, S. Duan, P. M. Radjenovic, Z.-Q. Tian, and J.-F. Li, Acc. Chem. Res. **53**(4), 729 (2020).
[55]M. L. Tseng, C. M. Chang, B. H. Cheng, P. C. Wu, K. S. Chung, M.-K. Hsiao, H. W. Huang, D.-W. Huang, H.-P. Chiang, P. T. Leung, and D. P. Tsai, Opt. Express **21**, 24460 (2013).
[56]Y.-F. C. Chau, C.-J. Lin, T. S. Kao, Y.-C. Wang, C. Ming Lim, N. T. R. N. Kumara, and H.-P. Chiang, Results Phys. **17**, 103168 (2020).
[57]M.-J. Sung, Y.-F. Ma, Y.-F. Chau, and D.-W. Huang, Appl. Opt. **49**, 920 (2010).
[58]Y.-F. Chou Chau, C.-T. Chou Chao, H. J. Huang, M. R. R. Kooh, N. T. R. N. Kumara, C. M. Lim, and H.-P. Chiang, Nanomaterials **10**, 493 (2020).
[59]Y.-F. Chou Chau, K.-H. Chen, H.-P. Chiang, C. M. Lim, H. J. Huang, C.-H. Lai, and N. T. R. N. Kumara, Nanomaterials **9**, 1691 (2019).
[60]Y.-F. Chou Chau, C.-T. Chou Chao, H. J. Huang, U. Anwar, C. M. Lim, N. Y. Voo, A. H. Mahadi, N. T. R. N. Kumara, and H.-P. Chiang, Results Phys. **15**, 102567 (2019).
[61]Y.-F. Chou Chau, J.-Y. Syu, C.-T. C. Chao, H.-P. Chiang, and C. M. Lim, J. Phys. D: Appl. Phys. **50**, 045105 (2017).
[62]D. Dai, J. Yang, Y. Wang, and Y.-W. Yang, Adv. Funct. Mater. **31**(1), 2006168 (2021).
[63]Y.-F. Chau, H.-H. Yeh, and D. P. Tsai, J. Electromagn. Waves Appl. **24**, 1621 (2010).
[64]C.-T. Chou Chao, Y.-F. Chou Chau, H. J. Huang, N. T. R. N. Kumara, M. R. R. Kooh, C. M. Lim, and H.-P. Chiang, Nanomaterials **10**, 1399 (2020).
[65]A. Derkachova, K. Kolwas, and I. Demchenko, Plasmonics **11**, 941 (2016).
[66]M. H. Nayfeh and B. Morton, *Electricity and Magnetism* (Dover, 2017), Vol. 1.